Article

Operational Reliability Analysis of Turbine Blisk Using an Enhanced Moving Neural Network Framework

Xiao Liang [1,2]**, Wei Sun** [1]**, Qingchao Sun** [1] **and Chengwei Fei** [3,*]

1 School of Mechanical Engineering, Dalian University of Technology, Dalian 116024, China; liangx123456163@163.com (X.L.); sunwei@dlut.edu.cn (W.S.); qingchao@dlut.edu.cn (Q.S.)
2 Commercial Aircraft Engine Co., Ltd., AECC, Shanghai 200241, China
3 Department of Aeronautics and Astronautics, Fudan University, Shanghai 200466, China
* Correspondence: cwfei@fudan.edu.cn

Abstract: As one of the key components of an aeroengine, turbine blisk endures complex coupling loads under a harsh operational environment so that the reliability of turbine blisk directly influences the safe operation of aeroengine. It is urgent to precisely perform the reliability estimation of a complex blisk structure. To address this issue, an enhanced Moving Neural Network Framework (MNNF) is proposed by integrating compact support region theory, improve sooty tern optimization algorithm (ISTOA), and Bayesian regularization strategy into artificial neural network. The compact support region theory is applied to select the efficient samples for modeling from the training samples set, the ISTOA is to determine the optimal compact support region, and Bayesian regularization thought is utilized to improve the generalization ability of neural network model. The operational reliability assessment of aeroengine blisk is performed with the consideration of transient loads to verify the proposed MNNF method. It is shown that the reliability degree of turbine blisk stain is 0.9984 when the allowable value is 5.2862×10^{-3} m. In line with the comparison of methods, the developed MNNF approach has 0.99738 in root means square error, 3.1634×10^{-4} m in goodness of fit, 0.423 s in modeling time, 99.99% in simulation precision, and 0.496 s in simulation time under 10,000 simulations, which are superior to all other methods (i.e., 99.96%, 99.91%, 99.93%, 99.97%, and 99.97% in simulation precision and 16.27%, 4.82%, 30.07%, 39.87%, and 23.59% in simulation efficiency, for the response surface method (RSM), Kriging, support vector machine (SVM), back propagation-artificial neural network (BP-NN), and BP-NN based on particle swarm optimization (BP-PSO) methods, respectively). It is demonstrated that the MNNF method holds excellent modeling and simulation performances. The efforts of this study provide promising tools and insights into the reliability design of complex structures, and enrich and develop reliability theory.

Keywords: enhanced moving neural network; compact support region; turbine blisk; reliability estimation; complex structures

1. Introduction

Structural systems are usually assembled with multiple components and endure complex time-varying loads during operation so that failure and accidents are easily caused. As one structural system, the turbine blisk of aeroengine assembled by turbine disk and turbine blades is affected by flow field, thermal field, and structural field during the operation process, which result in strain failure and unacceptable aircraft flight safety. To ensure the reliable operation of structures, it is necessary to implement the reliability analysis of turbine blisk.

In the reliability design of engineering structures, numerous methods have emerged. Qian et al. employed an improved Monte Carlo (MC) simulation to implement the structural reliability of crane rail beam under stochastic crane movements and irradiation conditions [1]. Jensen et al. discussed the application of MC simulation in the reliability

design of structural systems under stochastic excitation [2]. The MC method is developed based on the Bernoulli law of large numbers to improve the analytical accuracy with the sample size, which is unacceptable in calculation burden for the reliability evaluation of complex structures. Importance sampling [3,4], truncated importance sampling [5,6], linear sampling [7], and directional sampling methods [8,9] are explored to reduce the computation burden of the MC method. To further improve the efficiency of the reliability evaluation for complex structures, the moment methods are explored by numerous scholars. Ricardo et al. applied the first-order second-moment (FOSM) method to investigate the reliability analysis of steel elements subjected to fire [10]. Dey et al. adopted the advanced FOSM to address structural reliability assessment of pedestrian bridges [11]. In addition, various moment methods are explored for the reliability analysis of complex structures [12–14]. The moment methods are widely utilized in the reliability evaluation of complex structures due to unique computational advantage, but it is only applicable to the known limit state function. In this case, surrogate modeling methods provide an effective way to address the above-mentioned drawbacks, which can be divided into the response surface method (RSM) [15], the Kriging model [16], support vector machine (SVM) [17], and neural network [18]. Lehký et al. performed the reliability estimation of complex structures by using RSM [19]. Fei et al. studied the RSM to derive the probabilistic analysis of casing radial deformation [20]. Yu et al. developed the adaptive Kriging and weighted sampling for reliability assessment of engineering structures [21]. Teng et al. presented the weighted Kriging model to perform the reliability design of turbine blisk [22]. Roy et al. investigated the application of SVM in structural reliability analysis [23]. Chen et al. explored the SVM with a similarity selection strategy and genetic algorithm for the reliability evaluation of nose landing gear shock strut outer fitting stress [24]. Zhang et al. employed the polynomial chaos expansion approach to evaluate structural reliability [25]. Yang et al. discussed the reliability evaluation for stress-constrained continuum structures using the polynomial chaos expansion method [26]. The neural network methods have received widespread attention owing to their excellent approximation performance and robustness. Lu et al. introduced a hybrid artificial neural network model to address the reliability design of turbine blisk [27]. Song et al. studied the improved neural network approach to implement the probabilistic analysis of flexible mechanisms [28]. Obviously, compared to numerical methods such as MC methods and moment methods, surrogate methods are a high-efficiency technique and are widely focused and developed in structural reliability design. Meanwhile, the neural network method is one promising surrogate method due to excellent approximation performance and robustness. Although the above-mentioned neural network methods have outstanding computational advantages for solving unknown limit state functions, the existing methods face some shortcomings for the operation reliability design of turbine blisk under multi-physical fields, including (i) the plenty of relevant available information in complex working environment. So far, the known samples information is underutilized so that the reliability design of complex structures is ineffective. (ii) Under the influence of complex factors, invalid samples in acquired samples exist and seriously influence the modeling accuracy and efficiency of neural network methods. (iii) The generalization ability and overtraining in neural network modeling is too inadequate for the accuracy of reliability analysis, which is difficult to satisfy for engineering requirements.

To resolve the above issues, an enhanced Moving Neural Network Framework (MNNF) is developed in this paper by introducing extremum thought, compact support region theory, improved sooty tern optimization algorithm (ISTOA), and Bayesian regularization (BR) into an artificial neural network model. Extremum thought is applied to reasonably handle the transient process of turbine blisk responses. Compact support region theory is employed to acquire the important modeling information from sample set. The improved sooty tern optimization algorithm (ISTOA) is adopted to optimize the compact support region radius and obtain the optimal modeling samples. The Bayesian regularization is utilized to find the optimal weights and thresholds of the final artificial neural network model. Subsequently, the operational reliability analysis of aeroengine turbine blisk strain

under multi-physical fields is conducted to validate the applicability and effectiveness of the proposed MNNF method. The modeling and simulation performance advantages of the MNNF model are demonstrated by comparing it to RSM, Kriging, SVM, back propagation-artificial neural network (BP-NN), and BP-NN based on particle swarm optimization (BP-PSO) approaches.

In what follows, Section 2 presents the presented MNNF model for the reliability analysis of complex structures, involving structural reliability estimation procedures, MNNF mathematical modeling, and reliability approach with the MNNF. Turbine blisk reliability evaluation is implemented in Section 3, including deterministic analysis of turbine blisk, MNNK modeling for turbine blisk strain failure, and reliability analysis for turbine blisk strain. Section 4 verifies the MNNF method from modeling and simulation performance perspectives. The main conclusions of this study are summarized in Section 5.

2. Enhanced Moving Neural Network Framework for Reliability Evaluation

In this section, the MNNF approach is developed for the reliability evaluation of structures, involving structural reliability estimation procedures, MNNF mathematical modeling, and the reliability approach with the MNNF.

2.1. Structural Reliability Estimation Procedures with MNNF

Due to the weakness of the MC simulation and moment methods in the high computational burden and unknown limit state functions, the neural network model has become a commonly adopted mean for structural reliability analyses. To solve the problems of insufficient utilization of known sample information and inadequate generalization ability of traditional neural network model, the enhanced MNNF is presented by introducing the compact support region theory, ISTOA, and Bayesian regularization strategy into the artificial neural network model. In the developed approach, the compact support region theory is used to determine effective samples. The ISTOA is adopted to obtain the optimal radius of compact support region. The Bayesian regularization strategy is employed to solve the weights and thresholds of the neural network model. The reliability evaluation process of engineering structures via the proposed MNNF model is shown in Figure 1. As indicated in Figure 1, the reliability evaluation process of engineering structures with the MNNF model includes deterministic analysis, effective samples acquirement, MNNF modeling, and reliability evaluation. The specific steps are described as follows:

Step 1 Determine the study object of engineering structure, i.e., aeroengine turbine blisk stain failure.

Step 2 Construct the finite element (FE) analysis model, and set the constraints of deterministic analysis, and implement the deterministic analysis of turbine blisk.

Step 3 Determine the input variables and output responses, and obtain the samples by Latin hypercube sampling (LHS) approach and conduct deterministic analysis, and divide the acquired into training and testing samples [29].

Step 4 Select the effective training samples by the initial compact support region for modeling.

Step 5 Establish the relationship between the input variables and output response by the neural network based on effective training samples, and solve the model hyperparameters via BR algorithm.

Step 6 Verify the accuracy and efficiency of the established MNNF model. If the MNNF model prediction accuracy fails to satisfy engineering requirement, the radius of the compact support region is optimized by the ISTOA, which combines the sooty tern optimization algorithm and chaotic cross learning strategy. Then, **Step 4** is performed until the engineering requirements are satisfied. If it satisfies engineering requirements, **Step 7** will be conducted.

Step 7 Establish the limit state function based on the MNNF model, and calculate the reliability degree of engineering structures applying MC simulation technology to perform

a large number of simulations, and validate the simulation performance for reliability assessment to output the results of reliability estimations.
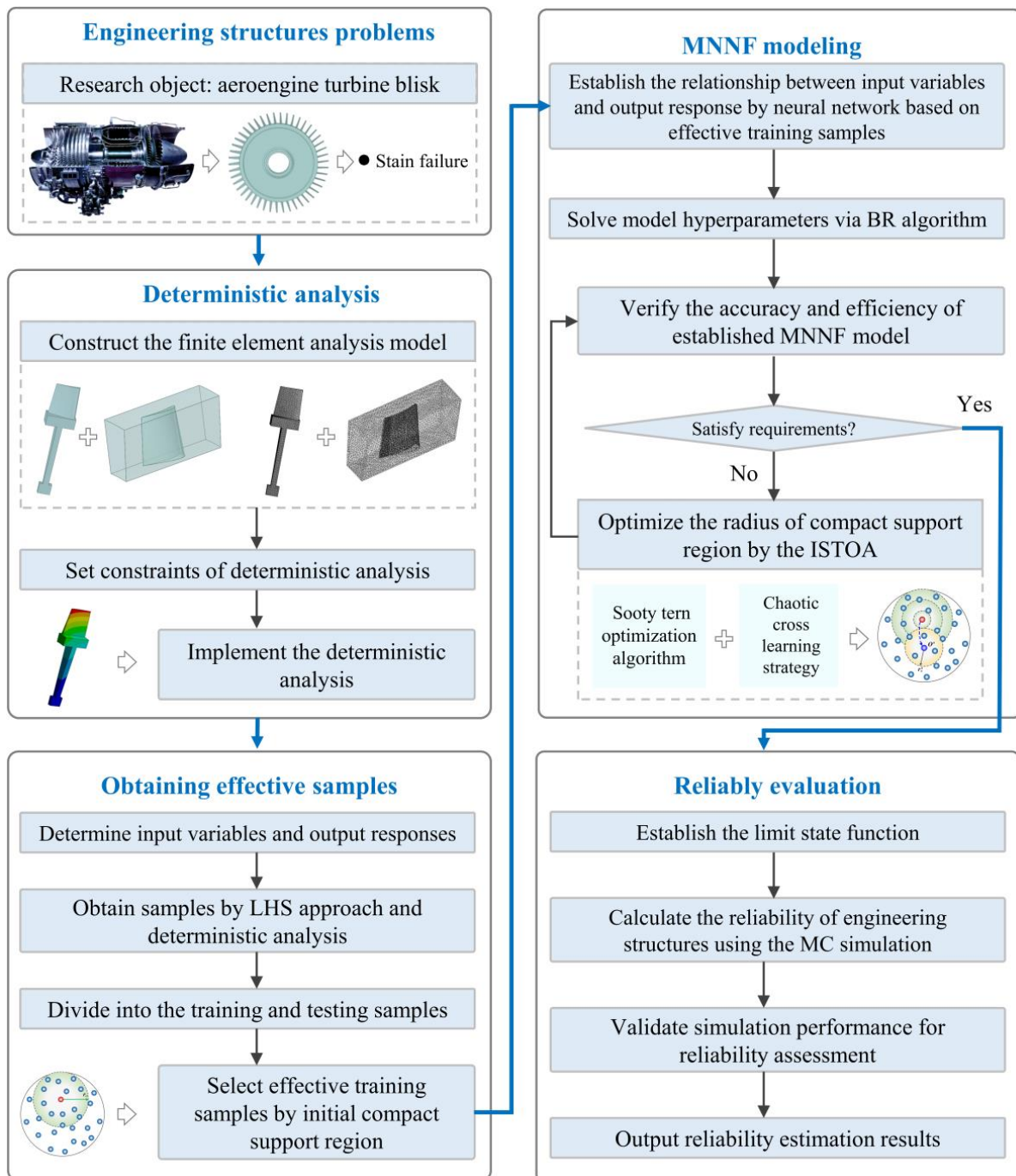
Figure 1. Reliability evaluation process of engineering structures using the MNNF model.

2.2. MNNF Mathematical Modeling

In this section, the MNNF model is presented by fusing the compact support region theory, artificial neural network, ISTOA, and Bayesian regularization strategy. To obtain a valid modeling information, the compact support region theory is introduced to select the effective samples (x, y) from the training samples $(x_{training}, y_{training})$. The two-dimensional schematic diagram of selecting the effective samples with the compact support region is depicted in Figure 2.
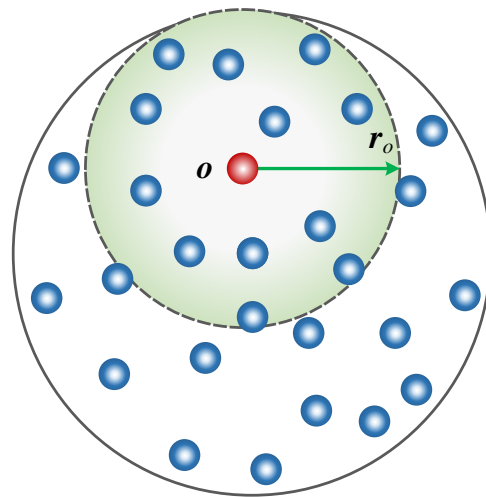
Figure 2. Schematic diagram of effective samples selection with the compact support region.

As displayed in Figure 2, one sample from the training samples is selected as a computation point *o*. The r_o is the initial radius of compact support region. The samples within the green area are considered as effective modeling samples.

Based on the selected effective modeling samples (x, y), the relationship between input variables and output response is established using the neural network model. The network structure of the MNNF model with the three-layer neural network is presented in Figure 3.
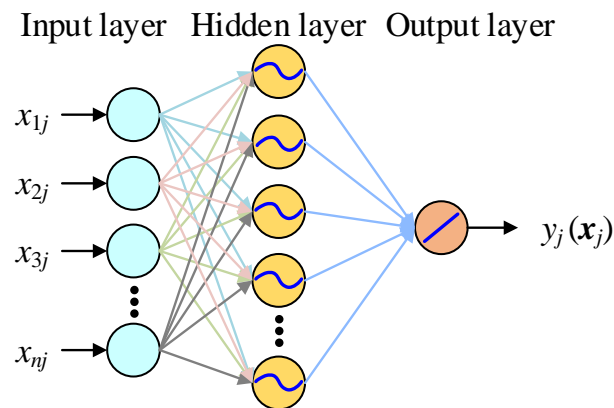
Figure 3. Network structure of the MNNF model with the three-layer neural network.

As shown in Figure 3, $x_j = \{x_{ij}\}$ ($i = 1, 2, \ldots, n$) is the *j*th input variable from effective modeling samples (training samples), which when served as the input layer, comprises *n* elements/input parameters $\{x_{ij}\}$ ($i = 1, 2, \ldots, n$). $y_j(x_j)$, which denotes the *j*th output response corresponding to the input variables $x_j = \{x_{ij}\}$ ($i = 1, 2, \ldots, n$), which is taken as the output layer. The hidden layer output y_h is expressed as [30]:

$$y_h = f_{hidden}\left(\sum_{h=1}^{s_h}\sum_{i=1}^{n} w_{iu}x_{ij} + \theta_u\right) \tag{1}$$

where *m* indicates the number of effective training samples; s_h represents the number of hidden layer neurons; w_{iu} is the connection weight between the *i*th input layer neuron and *u*th hidden layer neuron; θ_u is the *u*th threshold of hidden layer neuron; and f_{hidden} represents the activation functions of the hidden layer for the MNNF model.

The output layer y_{mnnf} can be denoted by:

$$y_{mnnf} = f_{output}\left(\sum_{v=1}^{s_o} w_{uv}y_h + \theta_k\right) = f_{output}\left(\sum_{v=1}^{s_o} w_{uv}f_{hidden}\left(\sum_{h=1}^{s_h}\sum_{i=1}^{n} w_{iu}x_{ij} + \theta_u\right) + \theta_k\right) \tag{2}$$

in which s_o is the number of output layer neurons; w_{uv} expresses the weight between the uth hidden layer neuron and the vth output layer neuron; θ_k indicates the kth threshold of output layer; and f_{output} represents the activation functions of output layer for the MNNF model.

The training error E_D of the MNNF model by the introduced compact support region is described as [31]:

$$E_D = \frac{1}{m}\sum_{j=1}^{m} W_c\left(y_{true} - y_{mnnf}\right)^2 \tag{3}$$

where y_{true} is the true value of effective training samples; W_c denotes the moving weighted for the MNNF model. The cubic spline function is adopted to determine the moving weighted W_c, i.e.:

$$W_c(o) = diag(w_c(o - x_1), w_c(o - x_2), \dots, w_c(o - x_m)) \tag{4}$$

$$w_m(o - x_j) = \begin{cases} \frac{2}{3} - 4\left(\frac{|o-x_j|}{r_0}\right)^2 + 4\left(\frac{|o-x_j|}{r_0}\right)^3, 0 < \frac{|o-x_j|}{r_0} < \frac{1}{2} \\ \frac{4}{3}\left(1 - \left(\frac{|o-x_j|}{r_0}\right)\right)^3, \frac{1}{2} < \frac{|o-x_j|}{r_0} < 1 \end{cases} \tag{5}$$

in which o represents the calculation point; $W_c(o)$ indicates the moving weighted matrix at calculation point o; and $w_m(o - x_j)$ and $|o - x_j|$ are the moving weighted and distance between calculation point o and jh efficient training sample, respectively.

To increase the generalization ability and avoid the overfitting of the MNNF model, Bayesian regularization strategy is adopted to gain the weights and thresholds. The training performance function is depicted as:

$$F(x, \xi) = \lambda E_w + \gamma\left(\frac{1}{m}\sum_{j=1}^{m} W_c\left(y_{true} - y_{mnnf}\right)^2\right) \tag{6}$$

where ξ is the undetermined weights and thresholds $\xi = [w_{iu}, \theta_u, w_{uv}, \theta_k]$; E_w represents the squares sum of MNNF weights; and λ and γ denote the regularization coefficients, i.e.:

$$\lambda = \frac{\varphi}{2E_w} \tag{7}$$

$$\gamma = \frac{m - \varphi}{2E_D} \tag{8}$$

where φ is the parameters number of effective training samples.

Then, the optimal weights and thresholds ξ^* can be described as:

$$\xi^* = \underset{\xi}{\arg\min} F(x, \xi) \tag{9}$$

If the established correlation model between the input variable and output response fails to meet the engineering requirements, the initial compact support region radius is changed. The two-dimensional schematic diagram of changing the compact support region radius is shown in Figure 4.
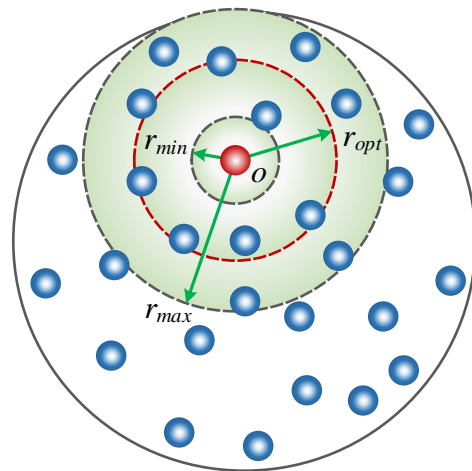
Figure 4. Schematic diagram of changing the compact support region radius.

Where r_{min} is the minimum radius of the compact support region that the minimum distance between the calculation points and the efficient training sample; r_{max} is the maximum radius of the compact support region, i.e., the maximum distance between calculation points and efficient training sample; and r_{opt} is the optimal radius of compact support region.

The intelligent algorithm is introduced to determine the optimal radius of the compact support region. The sooty tern optimization algorithm is widely used in optimization problems due to the strong ability of optimization [32]. However, the sooty tern optimization algorithm has the drawbacks of uneven initial population distribution and weak local search ability. Therefore, the chaotic cross learning strategy is integrated into the sooty tern optimization algorithm, to generate the chaotic sequence to increase the randomness of the initial population and utilize the poor position towards the superior position for cross-learning to expedite convergence. By the Tent chaotic mapping in n-dimensional space, the chaotic sequence $\boldsymbol{c}$ is acquired as:

$$\boldsymbol{c} = \begin{bmatrix} c_{11} & c_{21} & \cdots & c_{n1} \\ c_{12} & c_{22} & \cdots & c_{n2} \\ \vdots & \vdots & \ddots & \vdots \\ c_{1M} & c_{2M} & \cdots & c_{nM} \end{bmatrix} \tag{10}$$

where M represents population size. The chaotic mapping expression is indicated as:

$$c_{p+1,p} = \begin{cases} 2c_{pq}, 0 \leq c_{pq} < 0.5 \\ 2(1 - c_{pq}), 0.5 \leq c_{pq} \leq 1 \end{cases} \tag{11}$$

in which $p = 1, 2, \ldots, M$; $q = 1, 2, \ldots, n$. The initial population $\boldsymbol{IX}$ can be described as

$$\boldsymbol{IX} = \begin{bmatrix} IX_{11} & IX_{21} & \cdots & IX_{n1} \\ IX_{12} & IX_{22} & \cdots & IX_{n2} \\ \vdots & \vdots & \ddots & \vdots \\ IX_{1M} & IX_{2M} & \cdots & IX_{nM} \end{bmatrix} \tag{12}$$

The qth position of the pth initial population is indicated as:

$$\boldsymbol{IX}_{pq} = \boldsymbol{IX}_{\min q} + c_{pq}\left(\boldsymbol{IX}_{\max q} - \boldsymbol{IX}_{\min q}\right) \tag{13}$$

where $IX_{\max v}$ and $IX_{\min v}$ are the maximum and minimum value of IX_{pq}. The opposition initial solution OX can be denoted as:

$$OX_{pq} = IX_{\max q} + IX_{\min q} - IX_{pq} \tag{14}$$

To accelerate the convergence and avoid falling into a local optimum of sooty tern optimization algorithm, all positions are sorted according to the training performance function, which is divided into superior position and poor position groups. The poor position learns from the superior position by the cross-learning strategy. The principal diagram of poor position learning from superior position by cross-learning strategy is shown in Figure 5.
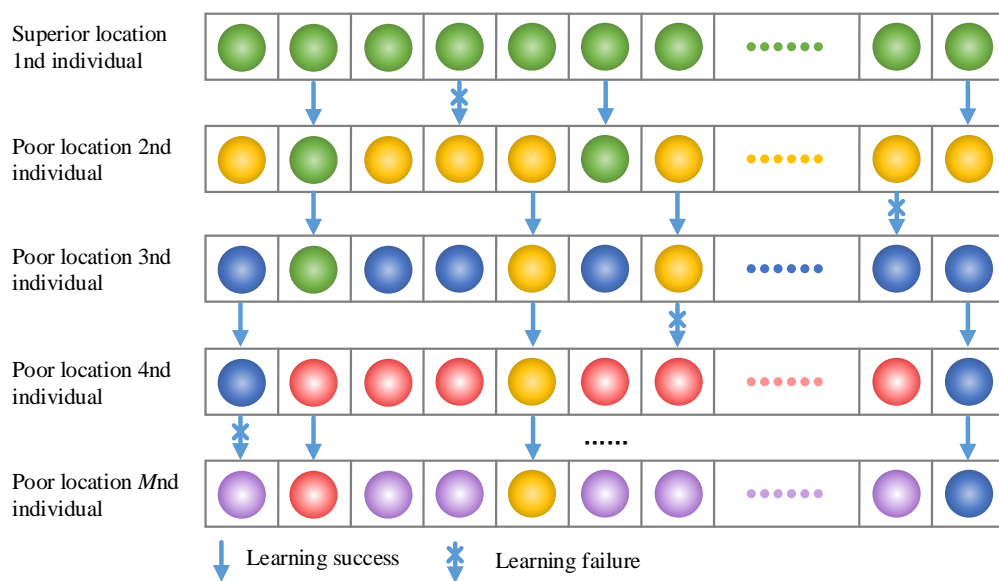
Figure 5. Principal diagram of poor position learning from superior position by the cross-learning strategy.

In Figure 5, the absolute differences are calculated between each individual in the poor position group and average dimension of the superior position group, and the dimensions with larger absolute differences are crossed. If the training performance function is small after crossing, the learning is successful, and otherwise is a failure, i.e.:

$$OX_{P,d} = \begin{cases} OX_{P,d}^k, F\left(OX_{P,d}^k\right) > F(OX_{P,d}) \\ OX_{P,d}, \quad \text{other} \end{cases} \tag{15}$$

where $OX_{P,k}$ is the dth individual for poor position group, $OX_{P,d}^k$ indicates the dth position after kth dimension learning crossover between $OX_{P,k}$ and the superior position group average dimension.

Then, the relationship between the input variables and output response is determined using the MNNF model, which provides theoretical support for the reliability analysis of engineering structures besides turbine blisk.

2.3. Reliability Approach with MNNF

In respect to the MNNF model, the limit state function h_{mnnf} of engineering structures is established as:

$$h_{mnnf} = y_{allow} - y_{mnnf} \tag{16}$$

in which y_{allow} indicates the allowable value of structural reliability estimation.

The failure probability P_f of structures is indicated by:

$$
\begin{aligned}
P_f &= \int_F f_X(\boldsymbol{x}) d\boldsymbol{x} = \int_{R^n} I_F(\boldsymbol{x}) f_X(\boldsymbol{x}) d\boldsymbol{x} = E[I_F(\boldsymbol{x})] \\
&= \frac{1}{N_{All}} \sum_{i=1}^{N_{All}} I_F(\boldsymbol{x}_i) = \frac{N_f}{N_{All}}
\end{aligned}
\tag{17}
$$

where N_{all} is the overall sample size; N_f represents the number of failed samples; $f_X(\boldsymbol{x})$ is the probability density function; and $I_F(\boldsymbol{x})$ is the indicator function of failure domain, which is described as:

$$
I_F(\boldsymbol{x}) = \begin{cases} 0, h_{mnnf}(\boldsymbol{x}) \geq 0 \\ 1, h_{mnnf}(\boldsymbol{x}) < 0 \end{cases}
\tag{18}
$$

where $I_F(\boldsymbol{x}) = 0$ and $I_F(\boldsymbol{x}) = 1$ denote the safe state and failure state, respectively.

The failure probability P_r of structures is expressed as:

$$
P_r = 1 - P_f
\tag{19}
$$

3. Reliability Assessment of Turbine Blisk with the MNNF Model

In this Section, the reliability assessment of aeroengine turbine blisk strain is implemented to verify the effectiveness of the developed MNNF model, involving the deterministic analysis of turbine blisk strain, the MNNK modeling for turbine blisk strain failure, and reliability analysis for turbine blisk strain.

3.1. Deterministic Analysis of Turbine Blisk

As an aircraft flight power device, aeroengine holds five work conditions comprising idle, take-off, climb, cruise, descent, and landing [33]. As a key component of an aeroengine, turbine blisk is prone to strain failure under long-term operation in extreme condition, which affects the performance and safety of aircrafts. To ensure the safe operation of aircrafts, it is urgent to conduct a reliability analysis of turbine blisk strain with the influence of flow field and structural field to guide the structural design of turbine blisks. In this study, the blisk with 46 blades assembled in one disk are selected as the object. Due to axial symmetry, 1/46 simplified blisk is considered to replace the whole blisk, for the analysis and simulation. With this way, the computational burden may be reduced to save the computational time and improve the computing efficiency. The fluid structure coupling solver is employed to calculate the strain of the turbine blisk, i.e., the Fluent and Transient modules are applied for flow field and structural field analysis, respectively. For the turbine blisk, the three-dimensional (3D) structural model and structural finite element (FE) with hexahedral cells and flow field finite volume (FV) model with tetrahedral elements are presented in Figures 6 and 7.
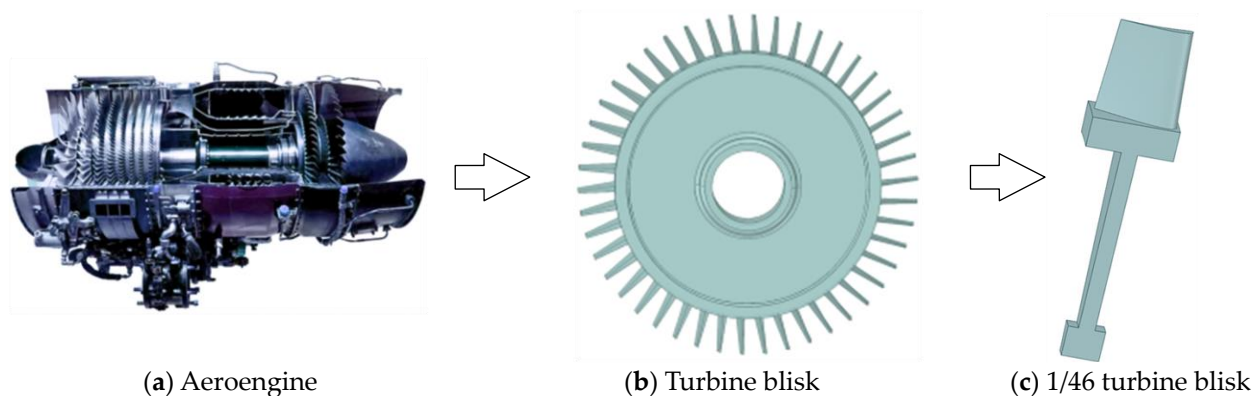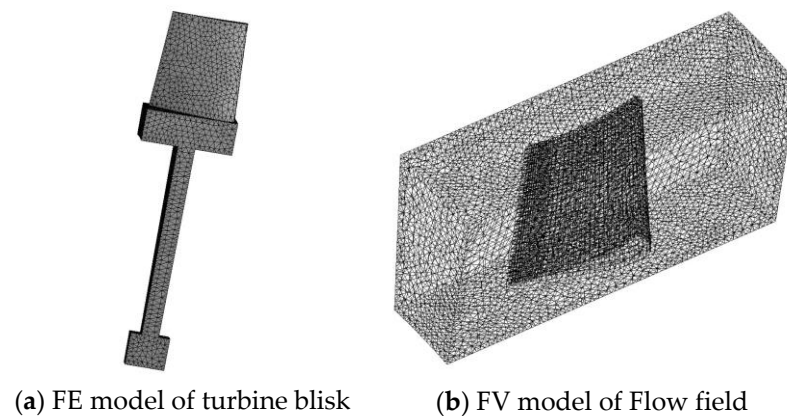

(**a**) Aeroengine   (**b**) Turbine blisk   (**c**) 1/46 turbine blisk

Figure 6. Aeroengine and the 3D models of turbine blisk.

(**a**) FE model of turbine blisk   (**b**) FV model of Flow field

Figure 7. FE and FV model of turbine blisk.

As illustrated in Figure 7, the model of turbine blisk includes 139,452 nodes and 76,569 tetrahedron elements. The FV model of Flow field contains 62,984 nodes and 331,246 elements. In this study, Nickel-based superalloy GH4133 is selected as the materials of the turbine blisk. The material performance parameters are listed in Table 1 [34].

Table 1. Material performance parameters.

Material Type	Parameter
Material name	Nickel-based superalloy GH4133
Density	8.56×10^3 kg/m^3
Elastic modulus	1.61×10^{11} Pa
Poisson ratio	0.3224

In the work condition, inlet pressure p_{in}, outlet pressure p_{out}, angular speed w, inlet velocity v, and density ρ are considered as the input variables of turbine blisk reliability analysis, while the blisk strain is regarded as output response. The time domain [0, 215 s] is simplified as the flight cycle of all stages for the deterministic and reliability analysis [35,36]. It is assumed that inlet pressure and outlet pressure are 2×10^6 Pa and 5.88×10^5 Pa, respectively [37]. The angular speed and inlet velocity varies in the time domain are indicated in Figure 8 [38].
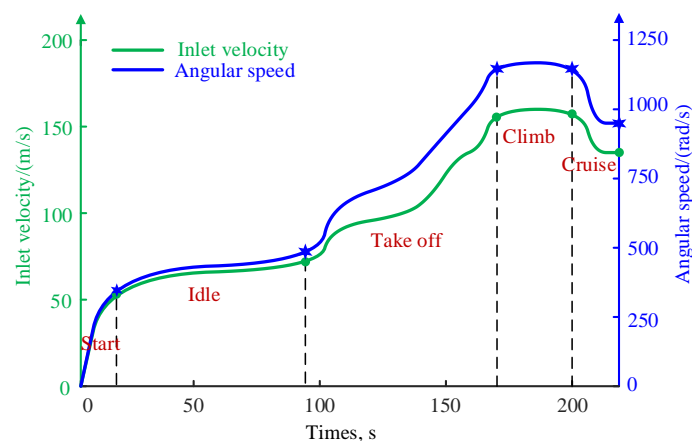
Figure 8. Angular speed and inlet velocity varies in the time domain. Blue stars and green circles indicate the key points in [0 s, 215 s] for angular speed and inlet velocity, respectively.
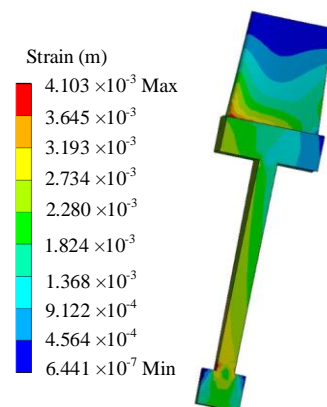
As illustrated in Figure 8, the time domain [0, 215 s] is divided into five stages of start, idle, take off, climb, and cruise. In respect to the above parameters and data, the deterministic analysis of turbine blisk is implemented. In this analysis, the maximum

strain of turbine bisk is obtained in the climb stage. The time point 190 s is selected as the computational point in this study. In the reliability analysis of turbine blisk, the distribution features of input variables at this time are shown in Table 2.

Table 2. Distribution features of input variables.

Input Variables	Mean	Standard Deviation
v, m/s	160	3.2
p_{in}, Pa	2,000,000	60,000
p_{out}, Pa	588,000	17,600
ρ, kg/m^3	8560	171.2
ω, rad/s	1168	23.36

Through the deterministic analysis of turbine blisk, the distribution of turbine blisk strain under fluid–structure coupling is displayed in Figure 9.

Strain (m)

4.103 ×10^{-3} Max
3.645 ×10^{-3}
3.193 ×10^{-3}
2.734 ×10^{-3}
2.280 ×10^{-3}
1.824 ×10^{-3}
1.368 ×10^{-3}
9.122 ×10^{-4}
4.564 ×10^{-4}
6.441 ×10^{-7} Min

Figure 9. Distribution of turbine blisk strain.

### 3.2. MNNK Modeling for Turbine Blisk Strain Failure

To structure the MNNK model, the LHS approach is adopted to extract 200 samples based on a deterministic analysis with regard to the distribution features of input variables in Table 2. Herein, 100 samples are regarded as training samples to establish the MNNF model, and the remaining 100 samples are considered as testing samples to verify the established model. The "5-5-1" three-layer neural network is regarded as the network structure of MNNF modeling.

In light of the 100 training samples, the compact support region is used to select the efficient training samples. The ISTOA is employed to the optimal compact support region radius, i.e., the number of efficient training samples is 82 within the optimal compact support region radius. The Bayesian regularization thought is adopted to solve the weights and thresholds of the MNNF model. The gained weights and thresholds of MNNF model are:

$$
\begin{cases}
w_{iu} = \begin{bmatrix}
-0.0275 & -0.0231 & -0.0037 & -0.8409 & -1.4315 \\
0.1859 & -0.0052 & 0.1278 & 0.9008 & -0.6572 \\
0.0014 & -0.0001 & 0.0004 & 0.1418 & 0.2357 \\
-0.9520 & 0.1330 & -1.4135 & -0.1667 & 0.5074 \\
0.0222 & -0.0046 & 0.0365 & -0.7270 & 0.5482
\end{bmatrix} \\
\theta_u = \begin{bmatrix} -1.5140 & -0.4217 & -0.2261 & -1.0124 & 1.6636 \end{bmatrix}^T \\
w_{uv} = \begin{bmatrix} -0.0620 & -0.0224 & 4.2067 & 0.0001 & 0.0979 \end{bmatrix} \\
\theta_k = 0.8508
\end{cases}
\tag{20}
$$

3.3. Reliability Analysis for Turbine Blisk Strain

Based on the established MNNF model of turbine blisk strain, a 2×10^4 MC simulation is performed to determine the allowable value. The distribution histogram and simulation history of turbine blisk strain are illustrated in Figure 10.


(**a**) Distribution histogram   (**b**) Simulation history
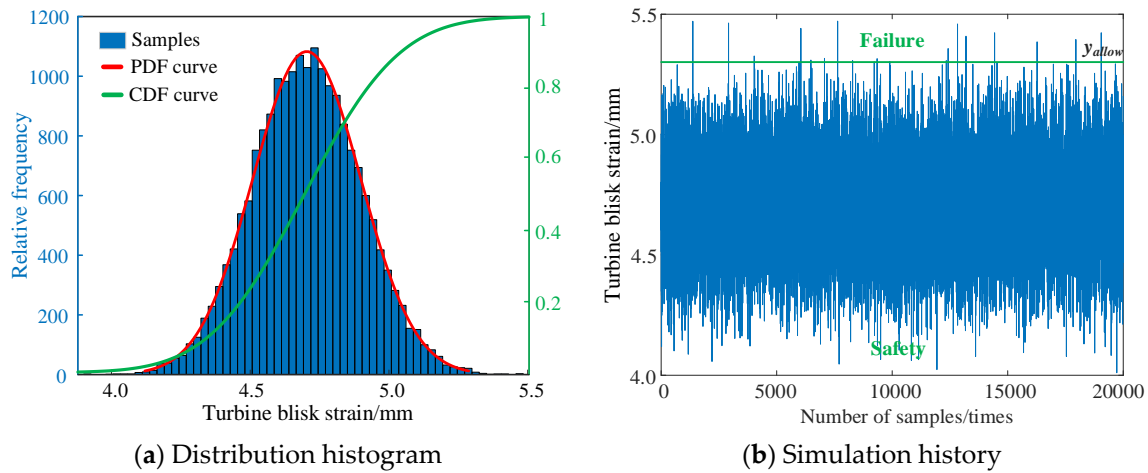
Figure 10. Turbine blisk stain distribution histogram and simulation history.

In Figure 10, the stain distribution of turbine blisk follows the normal distribution with the mean and standard variance being 4.7038×10^{-3} m and 1.9414×10^{-4} m, respectively. The allowable value of turbine blisk stain is determined to be 5.2862×10^{-3} m by the 3σ principle. The limit state function is determined based on the MNNF model, i.e.:

$$h_{mnnf} = y_{allow} - y_{mnnf} \tag{21}$$

According to the limit state function, different MC simulation times are performed to calculate the reliability of turbine blisk stain. The reliability variation curve is presented in Figure 11.
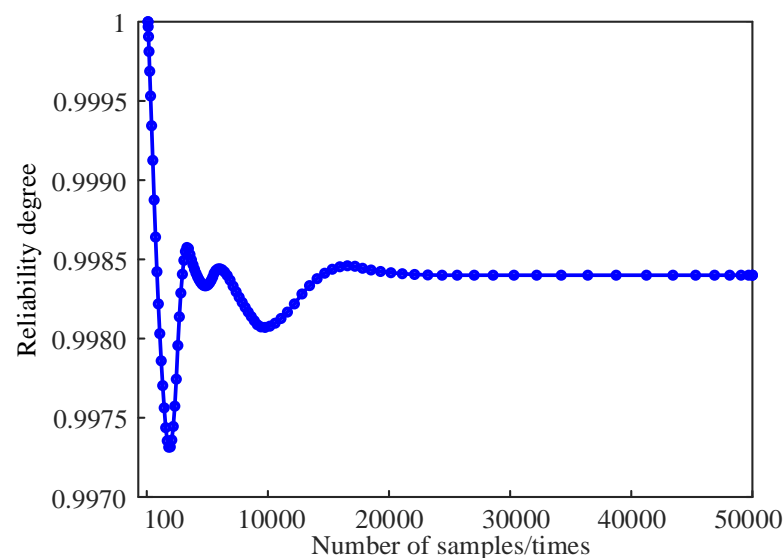
Figure 11. Reliability variation curve for turbine blisk stain.

As illustrated in Figure 11, the reliability degree of turbine blisk stain gradually converges to 0.9984 with the increase in MC simulation times.

4. Enhanced Moving Neural Network Framework Validation

The modeling properties and simulation performances of the MNNF model are verified by comparing it to the RSM, Kriging, SVM, BP-NN, and BP-PSO approaches. In addition, the hyperparameters of RSM, Kriging, and SVM are solved using least squares, gradient descent, and sequence minimum optimization methods. The network structures of BP-NN, BP-PSO, and MNNF are "5-5-1". In addition, the particle swarm optimization is used to solve the hyperparameters in the BP-PSO method. All calculations were performed in a 64-bit desk computer with Intel(R) Core (TM) i9-12900H 2.50 GHz CPU and 32 GB RAM (Intel, Santa Clara, CA, USA).

4.1. Modeling Properties

The root means square error (*RMSE*) and goodness of fit (*R*-Square, R^2) [30] are adopted as two evaluation indicators of the approximation performance of the MNNF modeling, i.e.:

$$\begin{cases} RMSE = \sqrt{\frac{1}{N_t}\sum_{l=1}^{N_t}\left(y_{true,l} - y_{mnnf,l}(\boldsymbol{x})\right)} \\ R^2 = 1 - \sum_{l=1}^{N_t}\left(y_{true,l} - y_{mnnf,l}(\boldsymbol{x})\right)^2 / \sum_{l=1}^{N_t}\left(y_{true,l} - y_{mnnf,l}(\boldsymbol{x})\right)^2 \end{cases} \tag{22}$$

where N_t is the number of testing samples, $y_{true,l}$ and $y_{mnnf,l}$ are the true value and approximate value of *l*th testing sample.

The RSM, Kriging, SVM, BP-NN, BP-PSO, and MNNF models are established using the training samples. In total, 100 testing samples are employed to evaluate the modeling properties of various methods. The modeling accuracy and modeling efficiency of six methods are shown in Figures 12 and 13.
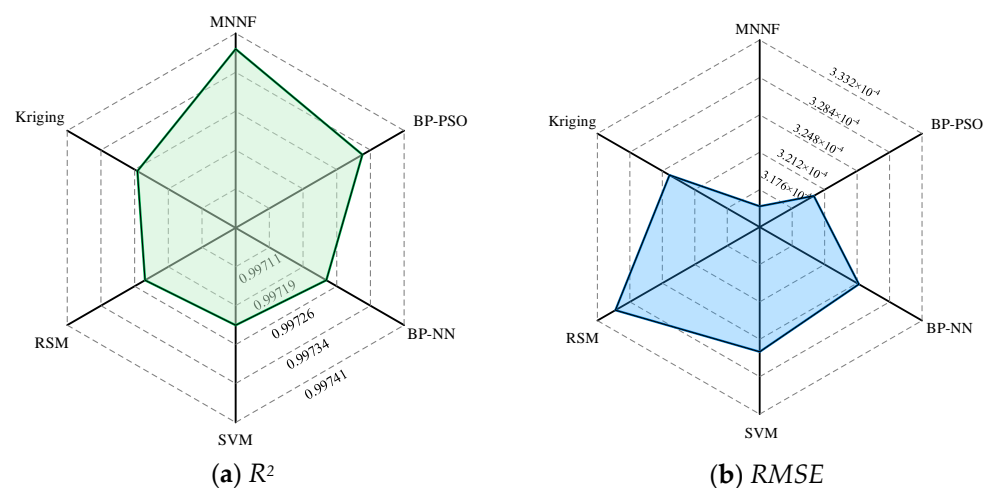

(a) *R²*

(b) *RMSE*

Figure 12. Taylor diagram for turbine blisk strain.

As indicated in Figure 12, (i) the R^2 of the MNNF model is 0.99738, which is closer to 1, comparing the other five methods; (ii) the *RMSE* of the MNNF model is 3.1634×10^{-4} m, which is smaller than other methods. Obviously, the modeling accuracy of the MNNF model is better than these of the RSM, Kriging, SVM, BP-NN, and PSO-BP approaches. As indicated in Figure 13, the modeling time of the MNNF model is 0.423 s, which is lower than other methods, and the modeling efficiency of the developed MNNF is improved by 60.99%, 83.94%, 87.90%, 33.33%, and 15.13% relative to RSM, Kriging, SVM, BP-NN, and BP-PSO, respectively. The MNNF model holds modeling advantages, resulting from two aspects: (i) the efficient modeling samples are obtained by the compact support region theory and the ISTOA to pledge the modeling accuracy and efficiency of MNNF; (ii) the
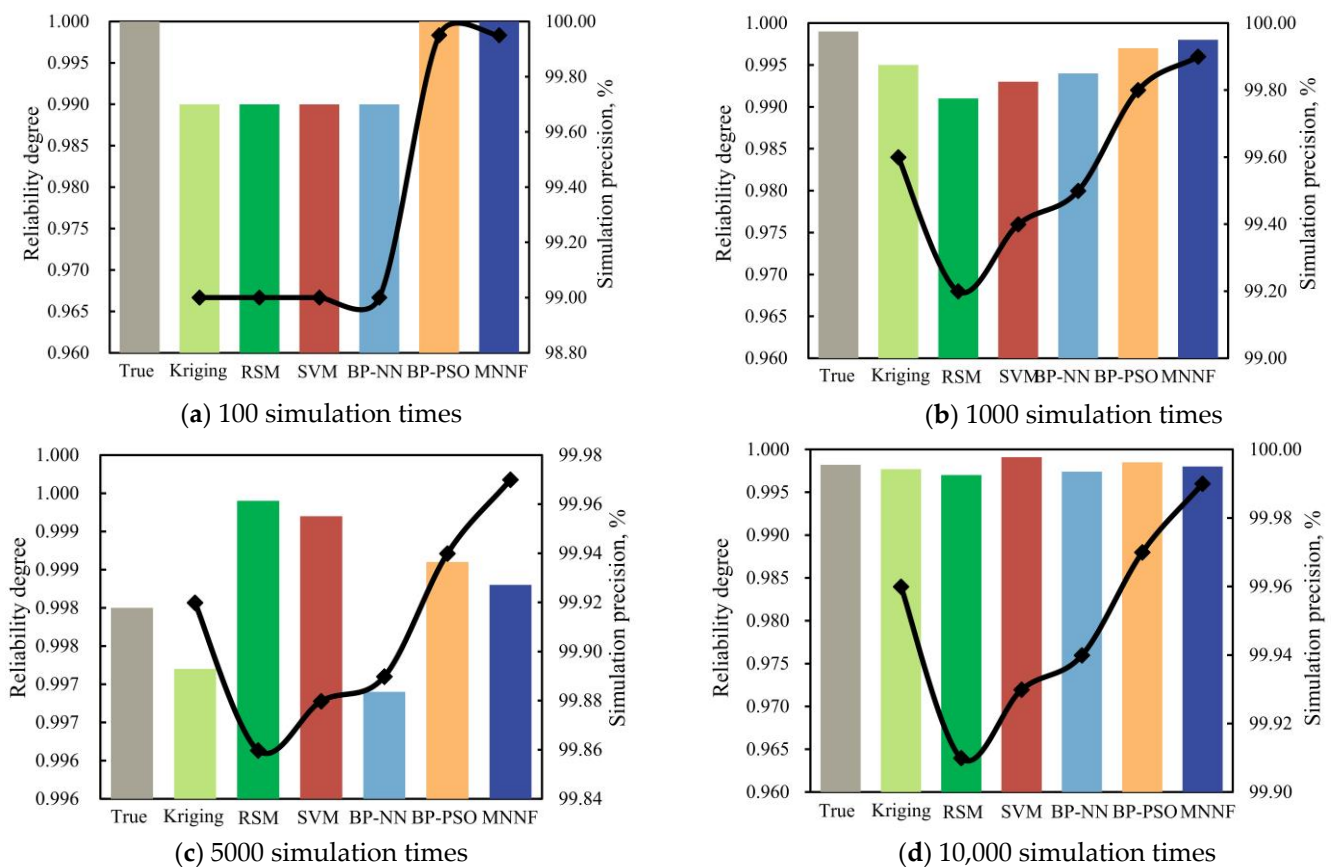
generalization ability is improved by the Bayesian regularization strategy for the modeling accuracy of MNNF.
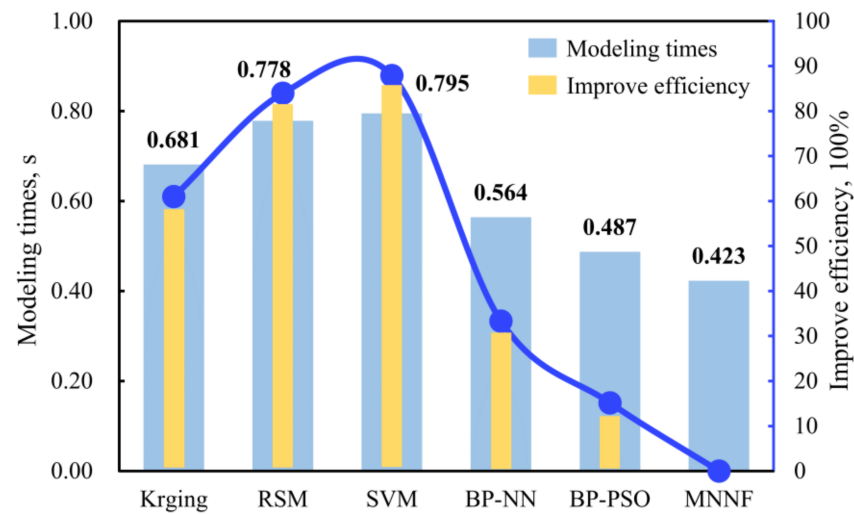
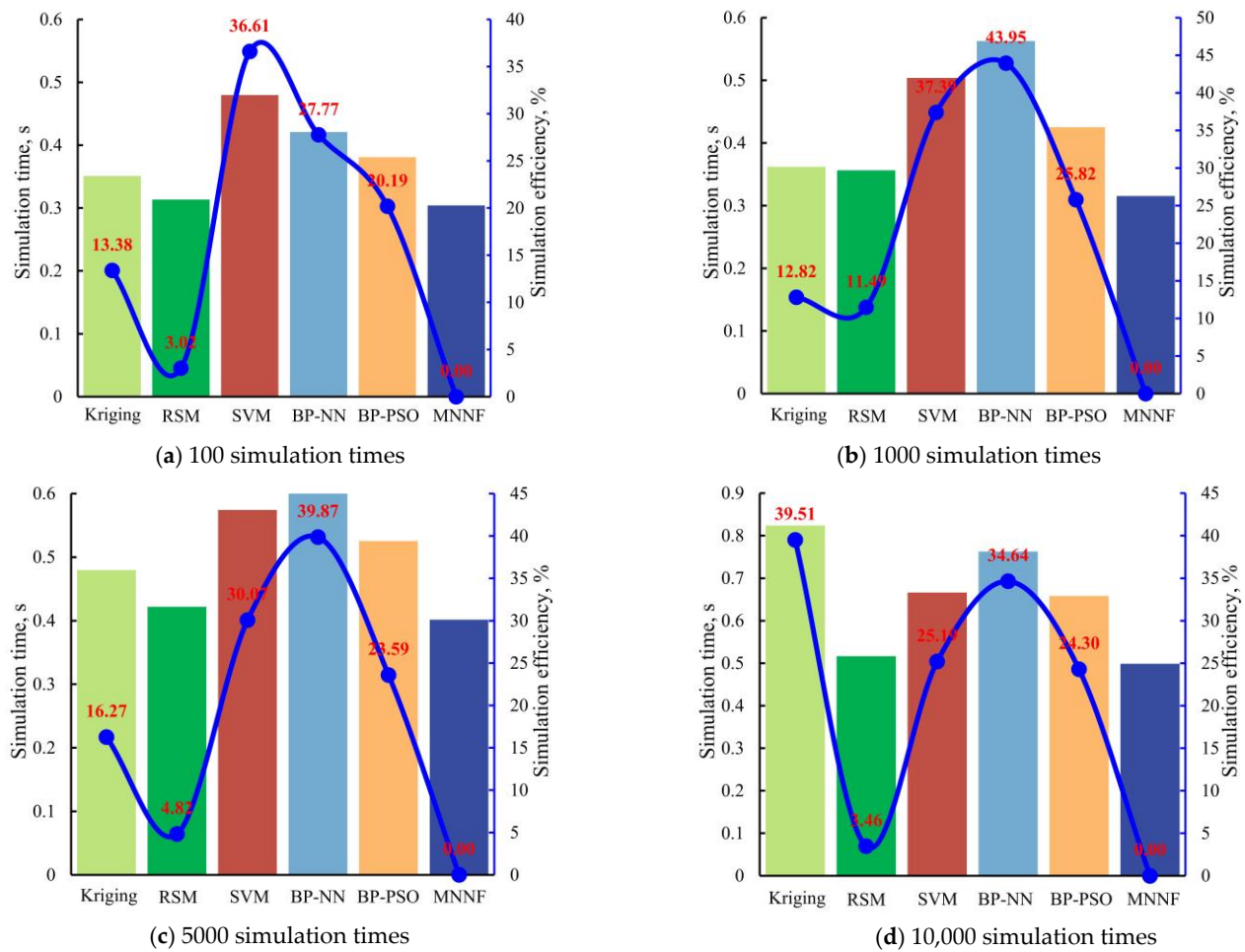**Figure 13.** Modeling efficiency of various methods.

4.2. Simulation Performances

In total, 100, 1000, 5000, and 10,000 MC simulations are implemented based on the limit state function of turbine blisk strain, respectively. The simulation precision and simulation efficiency of the six methods are displayed in Figures 14 and 15.

(**a**) 100 simulation times

(**b**) 1000 simulation times

(**c**) 5000 simulation times

(**d**) 10,000 simulation times

Figure 14. Simulation precision of different methods.

Figure 15. Simulation efficiency of different methods.

As presented in Figures 14 and 15, the simulation precision of the MNNF model is closer to the true reliability of turbine blisk strain, and the simulation efficiency is higher than other methods. The simulation precision of the RSM, Kriging, SVM, BP-NN, BP-PSO, and MNNF methods are 99.96%, 99.91%, 99.93%, 99.97%, 99.97%, and 99.99%, respectively, when the MC simulation times are 10 000. For the simulation efficiency, the computing time of MNNF is 0.496 s, which saves 16.27%, 4.82%, 30.07%, 39.87%, and 23.59% comparing to the RSM, Kriging, SVM, BP-NN, and BP-PSO models, respectively. The reason for the above results is attributed to the effective combination of compact support region theory, ISTOA, and Bayesian regularization strategy with the artificial neural network model.

Therefore, the proposed MNNF model has outstanding modeling properties and simulation performances in the reliability evaluation of turbine blisk strain.

5. Conclusions

The aim of this paper is to present the enhanced Moving Neural Network Framework (MNNF) for the operational reliability estimation of turbine blisk structure under multi-physical fields, i.e., fluid-structural coupling, by absorbing the compact support region theory, ISTOA, and Bayesian regularization strategy into an artificial neural network. In the developed method, compact support region theory is employed to choose the advantageous modeling samples from training samples. The chaotic cross-learning strategy is introduced to the sooty tern optimization algorithm for developing the ISTOA and then in optimizing the compact support region. Bayesian regularization thought is used to determine the weights and thresholds for enhancing the generalization ability. The reliability assessment

of aeroengine turbine blisk strain is implemented to verify the effectiveness of the MNNF model from an engineering perspective. The main conclusions are summarized as follows:

(i) The MNNF method is developed by introducing the compact support region theory, ISTOA, and Bayesian regularization strategy into the artificial neural network model for the reliability analysis of turbine blisk strain.

(ii) The reliability degree of turbine blisk strain is 0.9984 when the allowable value is 5.2862×10^{-3} m according to the reliability evaluation of turbine blisk strain with the proposed MNNF model.

(iii) The modeling properties of the MNNF model are verified by comparing the RSM, Kriging, SVM, BP-NN, and BP-PSO approaches. The modeling accuracy and efficiency with the RMSE of 0.99738, R^2 of 3.1634×10^{-4} m and modeling time of 0.423 s are superior to other methods.

(iv) The simulation performances of the MNNF model are demonstrated by different MC simulation times with multiple methods. The simulation precision of the MNNF model (99.99%) is higher than these of different approaches (i.e., RSM of 99.96%, Kriging of 99.91%, SVM of 99.93%, BP-NN of 99.97%, and BP-PSO methods of 99.97%. Compared with the RSM, Kriging, SVM, BP-NN, and BP-PSO methods, the simulation efficiency of the proposed MNNF is improved by 16.27%, 4.82%, 30.07%, 39.87%, and 23.59%, respectively.

The efforts of this study provide an effective method for the reliability assessment of complex structures besides turbine blisk, and enrich and develop mechanical reliability theory, which provides an insight for structural optimal design.

Nomenclature

MNNF	Moving Neural Network Framework
ISTOA	Improve sooty tern Optimization algorithm
MC	Monte Carlo
FOSM	First-order second-moment
RSM	Response surface method
SVM	Support vector machine
FE	Finite element
BP-NN	Back propagation-artificial neural network
BP-PSO	BP-NN based on particle swarm optimization
RMSE	Root means square error
R2	R-Square
LHS	Latin hypercube sampling

References

1. Qian, C.; Li, W.; Ren, Y.; Hu, Z.; Yang, L.; Zhao, X.; Wang, X. Monte-Carlo simulation-based analysis for structural reliability of the crane rail beam under stochastic crane movements and irradiation conditions. *Qual. Reliab. Eng. Int.* **2023**, *39*, 1704–1719. [CrossRef]
2. Jensen, H.A.; Jerez, D.J.; Valdebenito, M. An adaptive scheme for reliability-based global design optimization: A Markov chain Monte Carlo approach. *Mech. Syst. Signal Process.* **2020**, *143*, 106836. [CrossRef]
3. Tabandeh, A.; Jia, G.; Gardoni, P. A review and assessment of importance sampling methods for reliability analysis. *Struct. Saf.* **2022**, *97*, 102216. [CrossRef]
4. Tokdar, S.T.; Kass, R.E. Importance sampling: A review. *Wiley Interdiscip. Rev. Comput. Stat.* **2010**, *2*, 54–60. [CrossRef]
5. Qin, Q.; Cao, X.; Zhang, S. AWK-TIS: An improved AK-IS based on whale optimization algorithm and truncated importance sampling for reliability analysis. *CMES Comput. Model. Eng. Sci.* **2023**, *135*, 1457–1480. [CrossRef]
6. Zhang, H.; Song, L.K.; Bai, G.C. Moving-zone renewal strategy combining adaptive Kriging and truncated importance sampling for rare event analysis. *Struct. Multidiscip. Optim.* **2022**, *65*, 285. [CrossRef]
7. Song, J.; Wei, P.; Valdebenito, M.; Beer, M. Active learning line sampling for rare event analysis. *Mech. Syst. Signal Process.* **2021**, *147*, 107113. [CrossRef]
8. Zhang, X.; Lu, Z.; Cheng, K. AK-DS: An adaptive Kriging-based directional sampling method for reliability analysis. *Mech. Syst. Signal Process.* **2021**, *156*, 107610. [CrossRef]
9. Guo, Q.; Liu, Y.; Chen, B.; Zhao, Y. An active learning Kriging model combined with directional importance sampling method for efficient reliability analysis. *Probabilistic Eng. Mech.* **2020**, *60*, 103054. [CrossRef]
10. Ricardo, A.S.; de Santana Gomes, W.J. Structural reliability methods applied in analysis of steel elements subjected to fire. *J. Eng. Mech.* **2021**, *147*, 04021108. [CrossRef]
11. Dey, P.; Walbridge, S.; Narasimhan, S. Evaluation of design provisions for pedestrian bridges using a structural reliability framework. *J. Bridge Eng.* **2018**, *23*, 04017132. [CrossRef]
12. Breitung, K. SORM, design points, subset simulation, and Markov chain Monte Carlo. *ASCE-ASME J. Risk Uncertain. Eng. Syst. Part A Civ. Eng.* **2021**, *7*, 04021052. [CrossRef]
13. Lu, Z.H.; Hu, D.Z.; Zhao, Y.G. Second-order fourth-moment method for structural reliability. *J. Eng. Mech.* **2017**, *143*, 06016010. [CrossRef]
14. Zhao, Y.G.; Ang, A.H.S. On the first-order third-moment reliability method. *Struct. Infrastruct. Eng.* **2012**, *8*, 517–527. [CrossRef]
15. Teng, D.; Feng, Y.W.; Chen, J.Y.; Lu, C. Structural dynamic reliability analysis: Review and prospects. *Int. J. Struct. Integr.* **2022**, *13*, 753–783. [CrossRef]
16. Feng, G.; Wen, J.; Fei, C. LCF Lifetime Reliability Prediction of Turbine Blisks Using Marine Predators Algorithm-Based Kriging Method. *Aerospace* **2023**, *10*, 875. [CrossRef]
17. Afshari, S.S.; Enayatollahi, F.; Xu, X.; Liang, X. Machine learning-based methods in structural reliability analysis: A review. *Reliab. Eng. Syst. Saf.* **2022**, *219*, 108223. [CrossRef]
18. Fei, C.W.; Han, Y.J.; Wen, J.R.; Li, C.; Han, L.; Choy, Y.S. Deep learning-based modeling method for probabilistic LCF life prediction of turbine blisk. *Propuls. Power Res.* **2024**, *13*, 12–25. [CrossRef]
19. Lehký, D.; Šomodíková, M.; Lipowczan, M. A utilization of the inverse response surface method for the reliability-based design of structures. *Neural Comput. Appl.* **2022**, *34*, 12845–12859. [CrossRef]
20. Cheng, W.F.; Guang, C.B.; Tian, C. Extremum response surface method for casing radial deformation probabilistic analysis. *J. Aerosp. Inf. Syst.* **2013**, *10*, 47–52. [CrossRef]
21. Yu, S.; Wang, Z.; Li, Y. Time and space-variant system reliability analysis through adaptive Kriging and weighted sampling. *Mech. Syst. Signal Process.* **2022**, *166*, 108443. [CrossRef]
22. Teng, D.; Feng, Y.W.; Chen, J.Y. Intelligent moving extremum weighted surrogate modeling framework for dynamic reliability estimation of complex structures. *Eng. Fail. Anal.* **2022**, *138*, 106364. [CrossRef]
23. Roy, A.; Chakraborty, S. Support vector machine in structural reliability analysis: A review. *Reliab. Eng. Syst. Saf.* **2023**, *233*, 109126. [CrossRef]
24. Chen, J.Y.; Feng, Y.W.; Teng, D.; Lu, C.; Fei, C.W. Support vector machine-based similarity selection method for structural transient reliability analysis. *Reliab. Eng. Syst. Saf.* **2022**, *223*, 108513. [CrossRef]
25. Zhang, X.; Pandey, M.D.; Luo, H. Structural uncertainty analysis with the multiplicative dimensional reduction–based polynomial chaos expansion approach. *Struct. Multidiscip. Optim.* **2021**, *64*, 2409–2427. [CrossRef]
26. Yang, B.; Cheng, C.; Wang, X.; Bai, S.; Long, K. Robust reliability-based topology optimization for stress-constrained continuum structures using polynomial chaos expansion. *Struct. Multidiscip. Optim.* **2023**, *66*, 88. [CrossRef]
27. Lu, C.; Teng, D.; Keshtegar, B.; Alkabaa, A.S.; Taylan, O.; Fei, C.W. Extremum hybrid intelligent-inspired models for accurate predicting mechanical performances of turbine blisk. *Mech. Syst. Signal Process.* **2023**, *190*, 110136. [CrossRef]
28. Song, L.K.; Fei, C.W.; Bai, G.C.; Yu, L.C. Dynamic neural network method-based improved PSO and BR algorithms for transient probabilistic analysis of flexible mechanism. *Adv. Eng. Inform.* **2017**, *33*, 144–153. [CrossRef]
29. Xu, Z.; Wang, X. Global sensitivity analysis of the reliability of the slope stability based on the moment-independent combine with the Latin hypercube sampling technique. *Stoch. Environ. Res. Risk Assess.* **2023**, *37*, 2159–2171. [CrossRef]

30. Lu, C.; Feng, Y.W.; Teng, D. EMR-SSM: Synchronous surrogate modeling-based enhanced moving regression method for multi-response prediction and reliability evaluation. *Comput. Methods Appl. Mech. Eng.* **2024**, *421*, 116812. [CrossRef]

31. Shi, Y.; Behrensdorf, J.; Zhou, J.; Hu, Y.; Broggi, M.; Beer, M. Network reliability analysis through survival signature and machine learning techniques. *Reliab. Eng. Syst. Saf.* **2024**, *242*, 109806. [CrossRef]

32. Dhiman, G.; Kaur, A. STOA: A bio-inspired based optimization algorithm for industrial engineering problems. *Eng. Appl. Artif. Intell.* **2019**, *82*, 148–174. [CrossRef]

33. Pan, W.; Feng, Y.W.; Liu, J.Q. Parameter-Influencing Analysis of Aeroengine Operation Reliability. *J. Aerosp. Eng.* **2023**, *36*, 04023030. [CrossRef]

34. Teng, D.; Feng, Y.W.; Lu, C.; Keshtegar, B.; Xue, X.F. Generative adversarial surrogate modeling framework for aerospace engineering structural system reliability design. *Aerosp. Sci. Technol.* **2023**, *144*, 108781. [CrossRef]

35. Fei, C.W.; Li, H.; Lu, C.; Han, L.; Keshtegar, B.; Taylan, O. Vectorial surrogate modeling method for multi-objective reliability design. *Appl. Math. Model.* **2022**, *109*, 1–20. [CrossRef]

36. Lu, C.; Teng, D.; Chen, J.Y.; Fei, C.W.; Keshtegar, B. Adaptive vectorial surrogate modeling framework for multi-objective reliability estimation. *Reliab. Eng. Syst. Saf.* **2023**, *234*, 109148. [CrossRef]

37. Teng, D.; Feng, Y.W.; Chen, J.Y.; Liu, J.Q.; Lu, C. Multi-polynomial chaos Kriging-based adaptive moving strategy for comprehensive reliability analyses. *Reliab. Eng. Syst. Saf.* **2024**, *241*, 109657. [CrossRef]

38. Lu, C.; Fei, C.W.; Liu, H.T.; Li, H.; An, L.Q. Moving extremum surrogate modeling strategy for dynamic reliability estimation of turbine blisk with multi-physics fields. *Aerosp. Sci. Technol.* **2020**, *106*, 106112. [CrossRef]